The Meteoritical Society

Meteoritics & Planetary Science 48, Nr 1, 87–98 (2013)
doi: 10.1111/maps.12000

Application of nondestructive testing methods to study the damage zone underneath impact craters of MEMIN laboratory experiments

Dorothee MOSER[1,*], Michael H. POELCHAU[2], Florian STARK[1], and Christian GROSSE[1]

[1]Technische Universität München, Lehrstuhl für Zerstörungsfreie Prüfung, Baumbachstraße 7, 81245 München, Germany
[2]Albert-Ludwigs-Universität Freiburg, Institut für Geowissenschaften - Geologie, Albertstraße 23b, 79104 Freiburg, Germany
[*]Corresponding author. E-mail: moser@cbm.bv.tum.de

(Received 13 April 2012; revision accepted 18 September 2012)

Abstract–Within the framework of the Multidisciplinary Experimental and Modeling Impact Research Network (MEMIN) research group, the damage zones underneath two experimentally produced impact craters in sandstone targets were investigated using several nondestructive testing (NDT) methods. The $20 \times 20 \times 20$ cm sandstones were impacted by steel projectiles with a radius of 1.25 mm at approximately 5 km s^{-1}, resulting in craters with approximately 6 cm diameter and approximately 1 cm depth. Ultrasound (US) tomography and vibrational analysis were applied before and after the impact experiments to characterize the damage zone, and micro-computer tomography (μ-CT) measurements were performed to visualize subsurface fractures. The newly obtained experimental data can help to quantify the extent of the damage zone, which extends to about 8 cm depth in the target. The impacted sandstone shows a local *p*-wave reduction of 18% below the crater floor, and a general reduction in elastic moduli by between approximately 9 and approximately 18%, depending on the type of elastic modulus. The results contribute to a better empirical and theoretical understanding of hypervelocity events and simulations of cratering processes.

INTRODUCTION

Geophysical signatures belong to the most prominent features recognizable in impact craters on Earth. Often crater structures are first recognized due to the discovery of geophysical anomalies (e.g., Pesonen 1996). This is because most impact craters on Earth are either heavily eroded and thus are not directly recognizable by their surface expression (typical impact crater morphology) or they are buried by sediments and therefore not directly accessible (e.g., Donofrio 1997). Therefore, geophysical studies are an essential tool for identification and exploration of impact structures. Geophysical investigations may reveal shock-induced damage and fracturing beneath craters that can provide important information about the impact conditions if combined with other constraints such as crater dimensions and physical properties of the target obtained from field mapping. For example, in cases where terrestrial craters are heavily eroded or buried, geophysical measurements can be the only way to reconstruct the size of an event.

The nondestructive testing (NDT) methods applied here have similarities to geophysical methods applied in field studies. Typical geophysical methods to characterize terrestrial impact craters are gravity, magnetic, seismic, and electrical methods as well as geophysical investigation of drill cores (e.g., Pilkington and Grieve 1992). Laboratory and field measurements document that shock-induced damage of rocky target materials, like cracks and compaction, leads to a significant change of its ability to transmit sound waves, which in turn has a major effect on the propagation of the seismic energy during measurements (Pilkington and Grieve 1992; Ahrens and Rubin 1993; Xia and Ahrens 2001; Ai and Ahrens 2004, 2005; Ai 2006). The nature and degree of fracturing (complete brecciation or localized major faults) caused by an impact event determine the change in seismic velocities, measured geophysically in the field. For example, if a rock is highly brecciated with a large number of microcracks, its seismic velocity will be lower than for the same rock with an identical porosity and density, but containing a few large microcracks (Pilkington and Grieve 1992).

The MEMIN research group performed mesoscale hypervelocity cratering experiments (e.g., Poelchau et al. [2013] and references therein), with detailed real-time data acquisition (this work; ejecta dynamic studies, Hoerth et al. 2013), postmortem analyses (ejecta behavior, Sommer et al. 2013; crater dimension analysis, Dufresne et al. 2013; projectile-target interactions, Ebert et al. 2013) and numerical modeling of the experiments, and the material behavior (Güldemeister et al. 2013). The goal of this article is to define and characterize the subsurface damage zone created by two experimental impacts. One approach to analyze experimentally produced impact craters is to saw the targets in half and interpret the surfaces with macroscopic and microscopic techniques (e.g., Buhl et al. 2013; Dufresne et al. 2013; Kenkmann et al. 2011). The authors describe and analyze characteristic features such as terraced spall zones, concentric fracturing, and pervasive grain crushing toward the center. Cutting a target to investigate the damage zone bears a potential risk of introducing new cracks, which can obscure the results of the actual experiment (Ai and Ahrens 2004a). This problem can be eliminated by applying NDT methods.

In this article three NDT techniques are discussed: (1) ultrasound (US) tomography with through-transmission technique (postimpact), (2) micro-computer tomography (μ-CT) (postimpact), and (3) modal analysis for calculating the elastic moduli (pre and postimpact). A 3-D distribution of the variation in compressional (*p*-) wave velocity, measured with US, gives an outline of the fracturing in the interior of an impacted target. The micro-computer tomography analysis with X-rays can show differences in the density inside the target and the modal analysis is able to determine frequencies of the target's vibration after exciting it with a modal hammer. With this information the elastic moduli can be calculated.

EXPERIMENTAL SETUP

Impact Cratering Experiments

Hyper-velocity impact experiments were carried out at the facilities of the Ernst-Mach-Institute (EMI) in Freiburg, Germany, using a two-stage light-gas gun (for detail see Poelchau et al. 2013). In the present article the nondestructive evaluation of two nearly identical experiments with the lab codes A3-5124 and A8-5128 are presented. For the experiments, dry sandstone (Seeberger Sandstein) was chosen. The sandstone has a density of 2.05 ± 0.04 g cm^{-3} and a porosity of $23.1 \pm 0.5\%$ (Poelchau et al. 2013). Kenkmann et al. (2011) measured an elastic modulus of 14.8 ± 1.4 GPa for dry Seeberger sandstone. The targets had an edge-length of 20 cm and were impacted by 1.25 mm (radius) steel projectiles. The projectile (steel D-290-1, $\rho = 8.1$ g cm^{-3}) was accelerated to an impact velocity of approximately 5 km s^{-1} resulting in a kinetic energy of approximately 850 J.

For the impact experiments, the x–y plane ($z = 0$ cm) is defined as the impact surface. Z is positive underneath the crater surface. The crater center in experiment A3-5124 has the coordinates $x = 11.6$ cm, $y = 10.5$ cm, $z = 1.15$ cm. The shape of the crater rim is asymmetric with about 6.5 cm diameter in x direction and about 6 cm in y direction. The deepest point of the crater is 1.15 cm in z direction. For experiment A8-5128 the coordinates for the crater center are $x = 9.5$ cm, $y = 11.0$ cm, $z = 1.0$ cm. The shape of the crater rim is more symmetrical than in A3-5124 with approximately 5 cm diameter in x direction and y direction. The deepest point of the crater is 1.0 cm in z direction. Detailed information about the crater structure is given in Dufresne et al. (2013).

Nondestructive Testing

Ultrasound Tomography

The aim of US tomography is to measure the damage zone and fractures underneath the impact crater (Ai and Ahrens 2004a). Fractures and cracks are formed through plastic deformation and are distributed approximately hemispherically in the subsurface of the crater (e.g., Polanskey and Ahrens 1990; Ai 2006; Kenkmann et al. 2011; Buhl et al. 2013). The through-transmission ultrasound technique can characterize the interior of the target rock before and after the impact experiment, in a similar fashion as described by Xia and Ahrens (2001), Ai and Ahrens (2005), and Ai (2006).

To estimate the extent of the damage zone, all measurements were carried out in x, y, and z directions of the target (sandstone cube). For this, the surface of the target was divided into a grid with a spacing of 1 cm. A total of 1323 single US shots were performed for one tomography measurement with US transmitter and receiver on adjacent sides of the target. The transmitted frequency (20 kHz) was recorded with multi-resonant sensors. For measuring the travel time of the *p*-wave the recording was triggered by transmitting the signal. After measuring the first arrival of the *p*-wave the velocity of all measured 1323 US signals was calculated using the following equation:

$$v_p = s/t \tag{1}$$

where v_p is the *p*-wave velocity, s is the distance between transmitter and receiver (20 cm for straight ray paths), and t is the one-way travel time. With v_p values measured in the x, y, and z directions, a lower limit of v_p for each

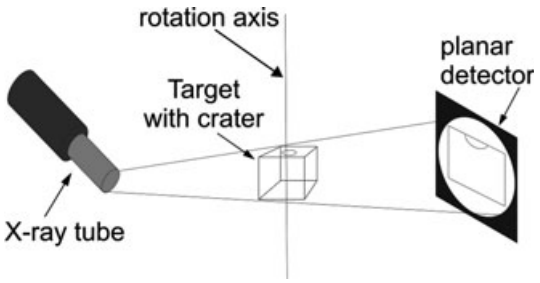

Fig. 1. Theoretical set-up for the micro-computer tomography measurements of an impacted target. The planar detector shows one 2-D measurement. For the 20 cm edge length sandstone target, the FOD (focus-object-distance) was 704 mm, the FDD (focus-detector-distance) was 1538 mm, the acceleration voltage was 280 kV, and the electrical current was 500 μA.

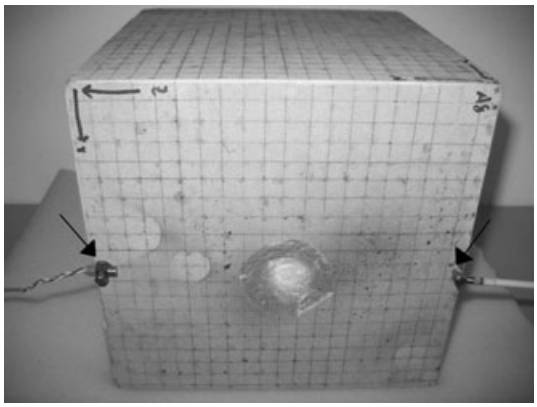

Fig. 2. Experimental set-up for the modal analysis of the impacted target A8-5128 with a triaxial acceleration sensor at the left and modal hammer on the right edge of the target (both indicated by arrows). This set-up is used to excite and measure the flexural vibration mode.

grid point within the target can be computed. The velocity of a grid point with *xyz* coordinates is calculated by the three individual measurements in *x*, *y*, and *z* direction that intersect at this point. All measurements are mean values of the whole travel path. As the measurement procedure with US sensors can alter and/or destroy the fragile crater surface, no measurements were performed in this area.

Micro-Computer Tomography Scanning

The motivation of the micro-computer tomography (μ-CT) is to resolve the dimensions of single cracks and to constrain the extent of the damage zone. The μ-CT measurements were carried out in cooperation with the Bundeswehr Research Institute for Materials, Fuels and Lubricants in Erding, Germany (WIWeB). For 3-D X-ray CT measurements several 2-D measurements with different view angles of the target were done. For that the target was rotated step wise, describing a full 360° rotation (Fig. 1). The X-rays permeate the target and impact the planar detector, located behind the target. On the detector they form a 2-D X-ray image. All 2-D images were then used to calculate a 3-D reconstruction (Michael 2001). A theoretical set-up for the μ-CT is shown in Fig. 1. The planar detector used in the μ-CT has a resolution of 2000×2000 pixels. The detector resolution in combination with the dimensions of the scanned block resulted in a scan resolution of around 140 μm per voxel (voxel = volume pixel), thus, limiting a detection of smaller cracks. The μ-CT measurements are an approach to visualize the fracture volume of the target. X-ray CT resolution can be greatly improved by using smaller samples. Therefore, it is planned to repeat the measurement with smaller targets.

Modal Analysis

In this study, modal analysis was utilized to record the natural resonant frequencies of vibrations of the MEMIN sandstone target to calculate the elastic moduli before and after the impact experiment. Previous studies have shown that the modal analysis is a good method of testing a damaged target, since damaging leads to a decrease in the elastic wave velocity and elastic moduli (Birch 1960; O'Connell and Budiansky 1974; Jones and Fącąoaru 1984; Weiler and Grosse 1995; Ai 2006; Ohtsu 2011). The changing frequencies of vibration expressed by the fundamental modes of longitudinal, flexural, and torsional vibrations of undamaged to damaged targets are related to changes in the configuration and stiffness of the target (Ohtsu 2011). Modal measurements do not give a localized resolution of the damage zone like the US tomography method. However, they provide an average damage estimate of the whole target (Ohtsu 2011). The elastic parameters can describe the structural behavior of the target. The parameter frequency, absorption factor, and the mode can describe the structural dynamics and the dynamic circumstances.

For the measurements, a modal hammer and a piezoelectric triaxial acceleration sensor were used (Fig. 2). The system converts the mechanical acceleration of the sensor into an electrical signal, so that a fast Fourier transformation (FFT) can be calculated to evaluate the frequency spectrum. The triaxial sensor is able to record information in *x*, *y*, and *z* directions. The maximal displacement of a sensor component is controlled by both the excitation point of the hammer and the properties of the tested material.

To obtain the natural frequencies the target has to be able to vibrate freely. Otherwise coupling effects with the surrounding area can falsify the results (Jones and Fącąoaru 1984; Weiler and Grosse 1995). In our case, foam material was used to limit coupling effects. The frequency peaks of the longitudinal, torsional, and

flexural modes are used to calculate the elastic moduli (Ohtsu 2011) using the following equations (Jones and Fąçąoaru 1984):

Torsional vibrations:

$$G_{\text{tors}} = \frac{f^2_{\text{tors}}}{k^2} * \frac{ml}{A} * 4 * R \quad (2)$$

Longitudinal vibrations:

$$E_{\text{long}} = \frac{f^2_{\text{long}}}{k^2} * \frac{ml}{A} * 4 * C \quad (3)$$

Flexural vibrations:

$$E_{\text{flex}} = \frac{f^2_{\text{flex}}}{(2k+1)^4} * \frac{ml}{I} * \frac{64}{\pi^2} * T \quad (4)$$

In these equations G and E denote the shear modulus [N mm^{-2}] and the elastic modulus [N mm^{-2}], respectively. k describes the dimensionless harmonic order, A [mm^2], m [kg], and l [mm] denote cross-section area, mass, and length of the target. I [kg*mm^2] denotes the moment of inertia of the cross-section of the target (for a rectangular section: $I = bh^3/12$; where b [mm] = width and h [mm] = height). R, C, and T are correction factors for the geometric dimensions of the target and f_{tors} [Hz], f_{long} [Hz], and f_{flex} [Hz] are the recorded torsional, longitudinal, and flexural frequencies.

RESULTS OF THE NDT EXPERIMENTS

Ultrasound Tomography

The US tomography revealed a remarkable distribution of the measured compressional wave velocities within the target (Figs. 3 and 4). The slices shown here are 3 out of 63 balanced calculations to visualize the whole target. Particularly the area around the impact crater is characterized by a significant reduction in the wave velocity down to 82% of the velocity measured in undamaged areas. As shown in Figs. 3a–c, the gradient of the velocity appears to be of roughly hemispherical nature. This low-velocity zone is interpreted as the damage zone and the results suggest a maximum depth of around 8 cm below the impacted surface. A nearly constant velocity with a small gradient was found for deeper layers (z = 8–20 cm) indicating more or less unaffected areas within the target.

Figures 4a–c show the measured velocity in x (Fig. 4a), y (Fig. 4b), and z (Fig. 4c) direction plotted against the shot points for individual US measurement series (also used for the 3-D US tomography). For each direction 21 series with 21 single shots and 1 cm spacing are measured (not all shown in Fig. 4). Every single

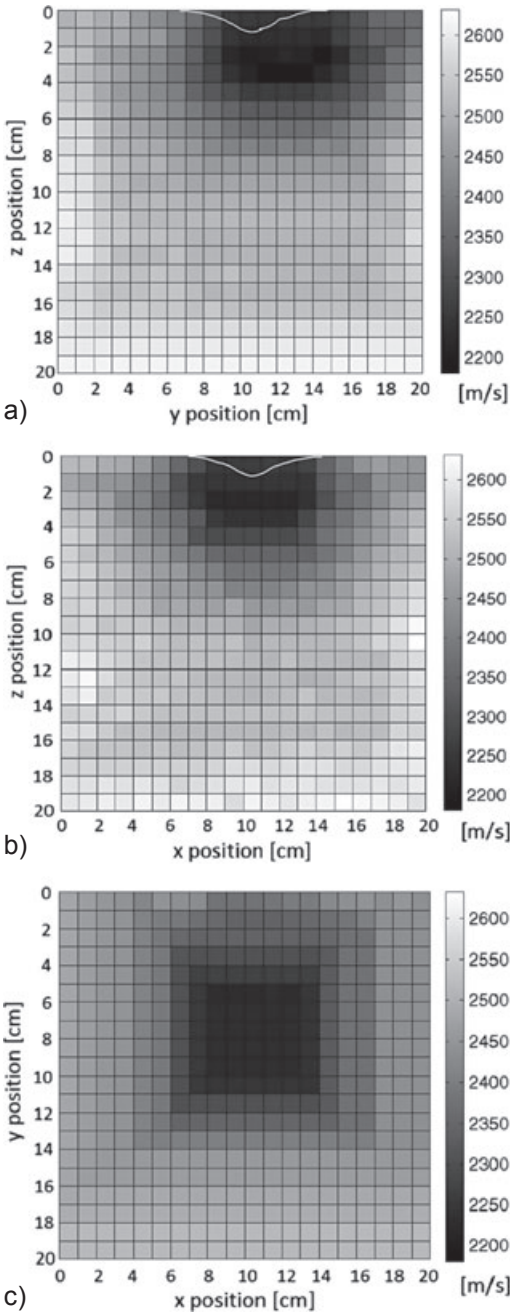

Fig. 3. 3-D calculation with 2-D ultrasound through-transmission measurements of the target A3-5124. The gray-scale map shows the p-wave velocity [m s^{-1}]. Dark shades, indicating the damage zone, have lower velocities than the surrounding sandstone matrix. The approximate crater position is indicated by a white line (more information about the crater morphology can be found in Dufresne et al. 2013). The figures show three cross-sections of the impacted target with 20 cm edge length. The x and y axis show the measured shot points for the through-transmission with one 1 cm offset. a) shows the y-z plane for x = 11 cm, b) shows the x–z plane at y = 10 cm, and (c) shows the x–y plane at z = 2 cm. The coordinates for the deepest point of the crater are x = 11.6 cm, y = 10.5 cm, and z = 1.15 cm.

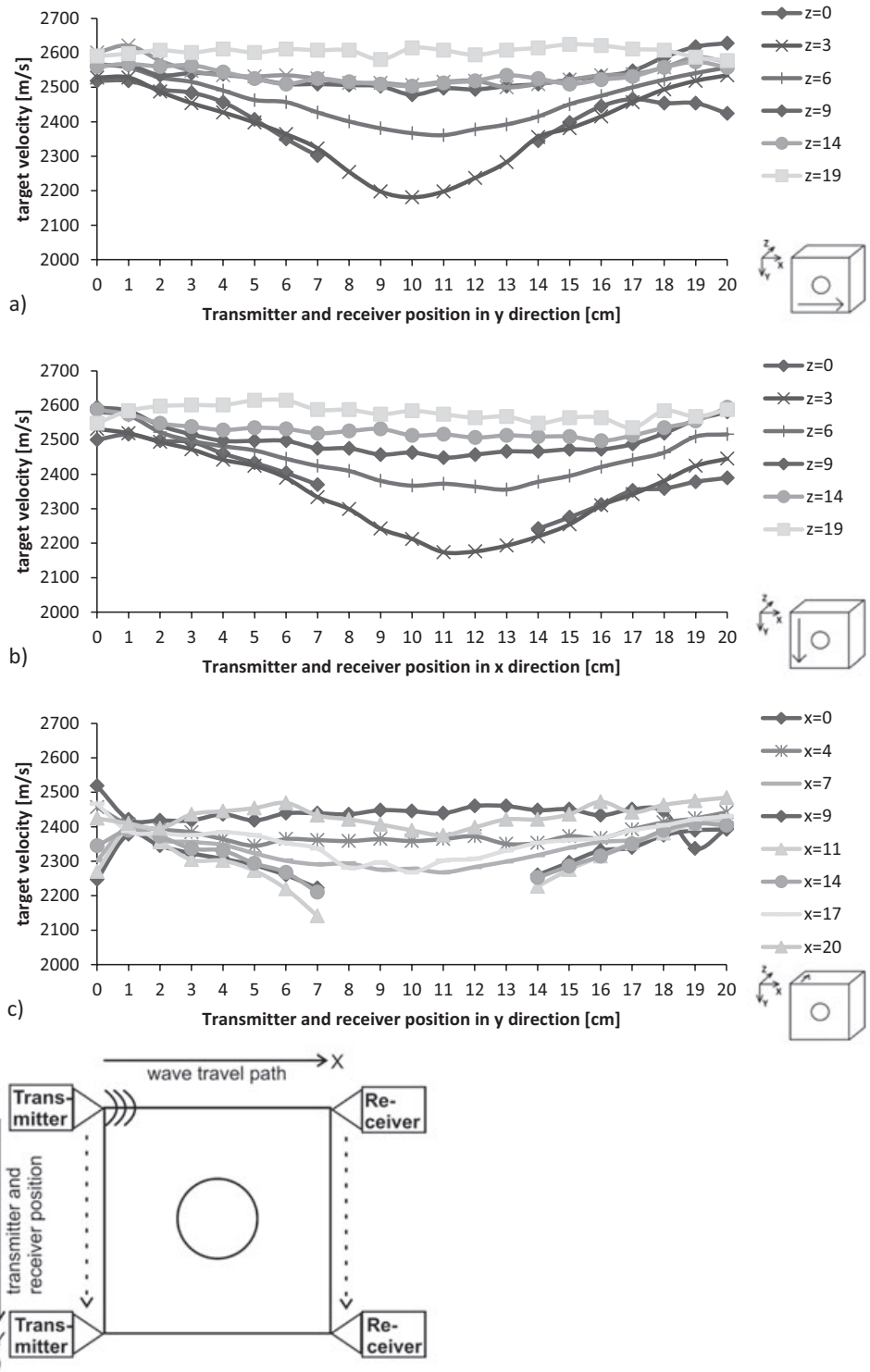

Fig. 4. Diagrams (a–c) show the distribution of the *p*-wave velocities within target block A3-5124. The abscissa indicates the position of the transmitter and the receiver along the surface for each series (compare Fig. 4d). The ordinate shows the measured *p*-wave velocity of the target. Based on the coordinate system of the target block shown at the bottom right, each diagram shows measurements with a different orientation of the wave travel path, indicated by the arrow inside the small block. No measurements were performed in the area of the crater, leading to gaps in the curves in 4c. In 4a and 4b the series $z = 0$ show no values between 9 and 14 cm because the wave travel path passes through the crater surface. Figure 4d shows the measurement setup for the results in Fig. 4a. The wave travel path is oriented in *x*-direction, based on the coordinate system of the target. The transmitter and receiver are then shifted 1 cm in *y*-direction for each new measurement.

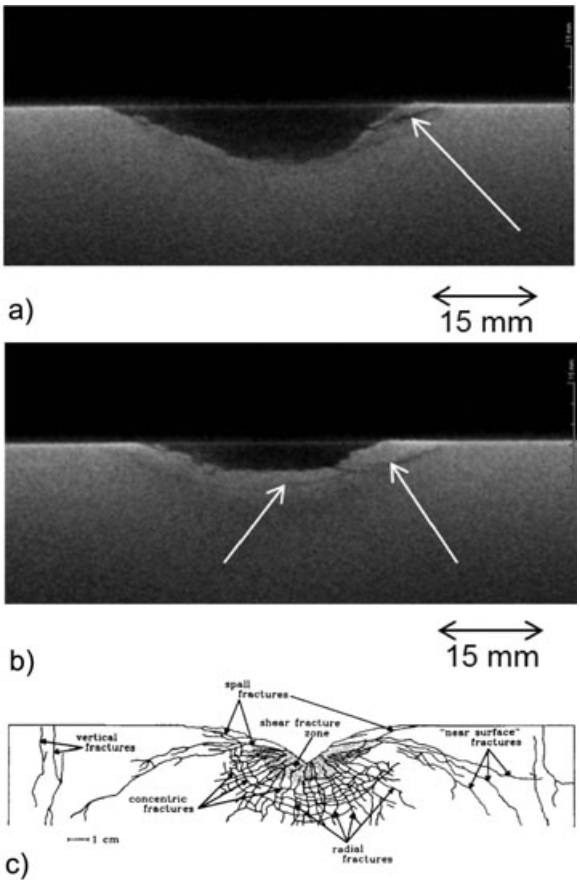

Fig. 5. (a) and (b) show two parallel cross-sections of a μ-CT measurement of the damaged sandstone target from experiment A3-5124. The white arrows indicate cracks underneath the crater surface: a) shows spall fractures running upwards toward the target surface, b) shows additional concentric fractures in the first cm underneath the crater surface, c) A cross-section of a gabbro target from Polanskey and Ahrens (1990) (shot 840904) illustrating a classification of internal fractures. The shaded zone underneath the crater indicates the highly fractured region. Compared to the μ-CT measurements in (a) and (b), the spall fractures have a similar position and expansion. Note that the downward trending "near surface" fractures are not visible in MEMIN experiments.

series shows results for a specific depth for Figs. 4a and 4b in increasing the z-direction. At a depth of 9 cm the velocity remains more or less constant in both the x and y directions. In Fig. 4c, series were recorded from the cratered target surface to the back of the target (i.e., in the z-direction). The crater center is 10.5 cm in the y-direction and the diameter is about 6 cm. No measurements were done within the crater to avoid damaging of the crater structure. An approximately constant velocity of the series is seen both between shot points 1 and 2 and between 19 and 21. The damage zone at the surface has a radial extent of about 7–8 cm from the center of the crater. In Fig. 4(c) the data for sensor position at 0 cm show a wide spreading in the calculated velocities. It is not clear which influence the boundary effect has for the velocity measurements in this case.

Table 1. Elastic moduli and shear modulus of sandstone target A3-5124 before and after impact.

	Undamaged target (N mm^{-2})	Damaged target (N mm^{-2})	Decrease in (%)	Damage parameter with frequencies
E_{long}	14559 ± 120[a]	13312 ± 100[a]	9	0.16
E_{flex}	15355 ± 350[a]	12553 ± 280[a]	18	0.28
G_{tors}	6769 ± 81[a]	6032 ± 72[a]	11	0.21

[a]Errors are standard deviation.

To test the reliability of the US tomography measurements and to obtain a reference value for the velocity of the pristine, undamaged sandstone target, measurements were performed at the center of each surface of the cube prior to the cratering experiment. With this data a damage parameter was calculated according to Ahrens and Rubin (1993):

$$D_p = 1 - (v_p/v_{p0})^2 \quad (5)$$

D_p is the damage parameter, v_p is the p-wave velocity, and v_{p0} is the p-wave velocity of the undamaged target. Undamaged targets should have a damage parameter value of 0, while highly damaged targets should approach values of 1. The highest damage measured in experiment A3-5124 is 0.44, using $v_p = 2181$ m s^{-1} and $v_{p0} = 2915$ m s^{-1} (measured before this sandstone block was impacted).

Results of the Micro-Computer Tomography

Results of micro-computer tomography scans are shown in Fig. 5. The images show the density of the present material. Darker shades represent lower density. Two individual profiles show cracks located below the crater surface (Figs. 5a and 5b). Cracks, smaller than 140 μm cannot be resolved. Similar to the results of Polanskey and Ahrens (1990) shown in Fig. 5c, the μ-CT visualizes several cracks and spall fractures (Figs. 5a and 5b) near the crater surface. Concentric fractures are also detectable with μ-CT measurements (arrow left side in Fig. 5b). The μ-CT only shows near surface fractures contrary to the cross-section of Polanskey and Ahrens (1990).

Results of the Modal Analysis

The modal analysis exhibits a significant reduction in the stiffness of the impacted target; three investigated vibration parameters (E_{long}, E_{flex}, and G_{tors}) reveal significantly decreased values (Table 1). The biggest

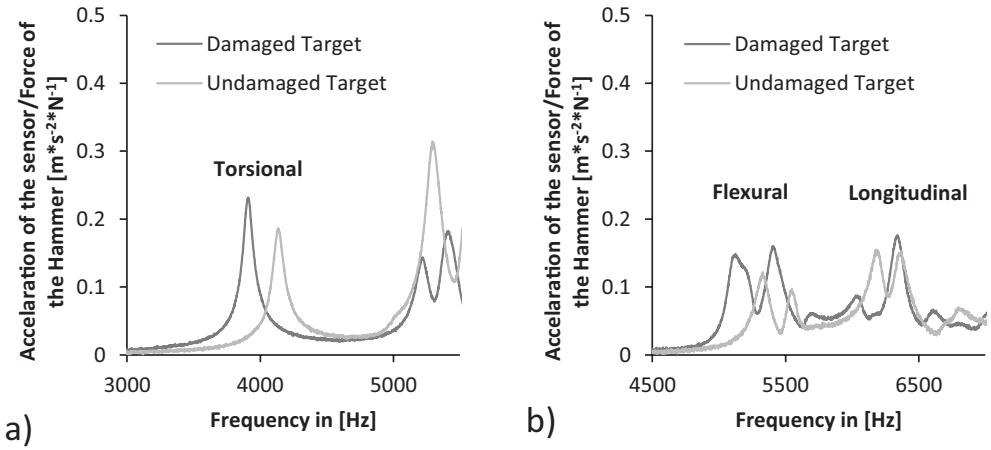

Fig. 6. Frequencies of a modal analysis with the undamaged (light gray) and damaged (dark gray) sandstone target block A3-5124. a) The peaks around 4000 Hz are torsional waves that are used to calculate the shear modulus. b) Peaks at around 5200 Hz are flexural waves and peaks at around 6200 Hz are longitudinal waves (not directly excited in this measurement). The frequency shift of the torsional, flexural, and longitudinal peaks to lower values is due to the damage caused by the impact. The *y*-axis shows the acceleration of the sensor [m s^{-2}] per unit of force excited by the hammer [N].

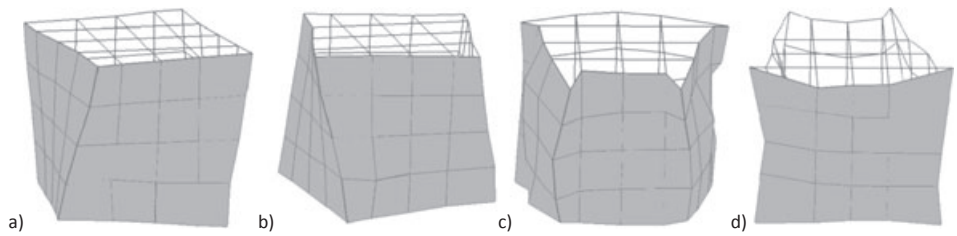

Fig. 7. Visualization of the fundamental eigenmodes of a target with 20 cm edge length. The grid indicates the measuring points for a full modal analysis. (a) and (b) show two maximal deflections of the torsional mode. (c) and (d) show two maximal deflections of the flexural mode.

difference was found for the flexural vibration value, which decreased by 18%. The values for the longitudinal and torsional vibrations are decreased by approximately 9% and 11%. In Fig. 6, the spectra of the modal analysis of a single measurement on the undamaged (light gray) and the damaged (dark gray) sandstone target are shown. These results make it clear that the damage caused by the impact changed the elastic parameters of the target. Figure 6a shows the frequencies measured with the triaxial sensor set to detect torsional vibrations. The peak at the lowest frequency (f_{tors} about 4000 Hz) is used to calculate the shear modulus G_{tors} after Equation 2. In Fig. 6b the frequencies measured with the triaxial sensor set to detect flexural waves are shown, giving an f_{flex} peak at approximately 5200 Hz. The sensor set-up for flexural waves (Fig. 6b) is not suited to measure torsional waves (Fig. 6a), because the sensors are located in one of the nodal points of flexural waves in this set-up. Therefore, no frequency peak is recognizable for f_{tors} at about 4000 Hz in Fig. 6b.

Frequencies in Fig. 6 are shifted toward lower values for the damaged target, due to the dampening effect of damaged rock on wave oscillations. Therefore, single measurements were used at which all vibration modes were excited separately to get a clear peak for each mode.

For a full modal analysis, measurements of all points of a defined grid are needed. With this information the vibration modes of the target can be visualized as shown in Fig. 7.

DISCUSSION

Hyper-velocity impacts have extreme consequences for the target (and the projectile, e.g., Ebert et al. 2013; Kenkmann et al. 2013). For the impacted target the damage is clearly visible. The energy released into the target and projectile resulted in shock-induced deformation and fracturing. For the cases discussed here, the calculated kinetic energy is 838 J, and the peak impact pressure is 63 GPa (Poelchau et al. 2013). This produces damage both at the surface and inside the target (seen in Figs. 3–5) and thus modifies the target characteristics (like the *p*-wave velocity [Figs. 3 and 4], and the elastic moduli [Table 1]).

Comparison of NDT Results with SEM Analysis

The extent of damage in the US profiles was compared with scanning electron microscopy (SEM) results of sections from another MEMIN impact experiment with comparable impact conditions (experiment A6-5126; Buhl et al. 2013). The target block was sawn in half after the experiment and thin sections of the crater profile were made for analysis. Microscopic fractures were mapped using the SEM images. It was found that the extent of fractures in the crater subsurface identified by SEM analysis is much smaller than in the ultrasound profiles (Fig. 4). The visible extent of damage is in the order of 1.7 cm beneath the preimpact surface, compared to 8 cm in the ultrasound profiles, suggesting that damage that occurs in the target cannot be visually detected on the μm-scale.

Comparison with Other Studies

In Table 2, experimental conditions, absolute damage depth, normalized damage depth r/r_p (the ratio of damage depth to projectile radius; Ai 2006), and several other parameters for a number of cratering experiments are given. Two tomographic methods, similar to our own method, were applied to determine the damage zone underneath experimental impact craters by Ahrens and Rubin (1993), Xia and Ahrens (2001), Ai and Ahrens (2004a, 2005), and Ai (2006). Both methods are based on US techniques; however, their approach is not nondestructive. The first method requires cutting a target into 1 cm cubes to locally determine the *p*-wave velocity, using US measurements with a transducer for generating the US signal and a receiver. The result of this so-called dicing method (Ahrens and Rubin 1993; Xia and Ahrens 2001) shows a decrease in *p*-wave velocity and thus damage with distance to the impact crater. In the second method, the target was cut into 1 cm thick slices and measured tomographically. A mechanical source was used to generate an elastic wave and the travel time was determined using a pair of transducers for the 1 cm thick slices (Xia and Ahrens 2001). For this method, the time interval between the recorded arrival times was evaluated. In comparison, for the nondestructive US tomography used in our study, an electrical source generated the elastic wave, so that the direct *p*-wave can be used for the calculated velocities. The results of Xia and Ahrens (2001), Ai and Ahrens (2004a, 2005), and the US tomography of MEMIN were all obtained through ultrasound measurements.

The two methods discussed in Xia and Ahrens (2001) show comparable damage depths (3.5 and 3.0 cm for the same target, experiment Xia & Ahrens shot 110). Xia and Ahrens (2001) performed three experimental shots into San Marcos gabbro target using aluminum spheres. Ai and Ahrens (2004a) impacted a San Marcos granite target with a lead bullet. Similar experiments with San Marcos gabbro and Fe sphere projectiles by Polanskey and Ahrens (1990) were evaluated by Ai (2006). The difference between the results of all these experiments (cf. Table 2) can be explained by differences in impact velocity (Xia and Ahrens 2001: 758–1019m s^{-1}; Ai and Ahrens 2004a: approximately 1200 m s^{-1}; MEMIN: 5000–5100 m s^{-1}), impact energy (Xia and Ahrens 2001: 71–129 J; Ai and Ahrens 2004a: 751 J; MEMIN: 838–873 J), as well as by differences in the material properties of the target rock and projectile. In particular, the 23% porosity of the Seeberger sandstone has a severe dampening effect on the shock wave and on the resulting experimental craters (e.g., Buhl et al. 2013; Güldemeister et al. 2013; Poelchau et al. 2013), and is expected to also have an effect on subsurface damage. It should be noted that the sandstone used in MEMIN is less dense (2.05 g cm^{-3}, Poelchau et al. 2013) than the gabbro used for the experiments of Xia and Ahrens (2.9 g cm^{-3}, Polanskey and Ahrens 1990).

To compare the results of these studies, r/r_p is plotted against the impact velocity (Fig. 8a) as well as against the impact energy (Fig. 8b), using the values from Table 2, including the visual damage characterization from Buhl et al. (2013) and information about the Meteor Crater in Arizona (Ackermann et al. 1975; Roddy et al. 1975) in Fig. 8a. The normalized damage depth of the MEMIN experiments, calculated with US tomography results, is much higher than results from visually evaluated experiments, as well as experiments with lower impact velocities evaluated by US. An increase in damage depth with impact velocity as well as with impact energy is seen for the experimental results measured with ultrasound (Fig. 8, dashed line). An increase in the damage depth in experimental results with visual evaluation is seen with a more flat gradient (Fig. 8, dotted-dashed line). More impact experiments in sandstone with an impact velocity between 1200 and 5000 m s^{-1} are needed for a better evaluation.

Damage Evaluation at Terrestrial Impact Craters

For terrestrial crater structures US tomography is not feasible. Most geophysical information is obtained by seismic refraction surveys (Ackermann et al. 1975; Pilkington and Grieve 1992; Ahrens and Rubin 1993). Meteor Crater in Arizona is a well preserved and thoroughly investigated terrestrial impact structure. The diameter of the crater is about 1.2 km and geophysical measurements (seismic refraction) detected a zone of fractured rock at least 800 m below the target surface (Ackermann et al. 1975; Roddy et al. 1975). For Meteor

Table 2. Damage depths and various parameters for impact cratering experiments of different studies.

Experiment	D_d(cm)	Projectile material	r_p (mm)	m_p (g)	Target material	m_t (g)	ρ (g cm^{-3})	v_i (m s^{-1})	E (J)	D_d/r_p
MEMIN A3-5124	9 (US)	D290-1 Steel	1.25	0.0670	Seeberger Sandstein	16400	2.05	5000	838	72.0
MEMIN A6-5126	1.7 (SEM)	D290-1 Steel	1.25	0.0671	Seeberger Sandstein	16400	2.05	5100	873	13.6
MEMIN A8-5128	8 (US)	D290-1 Steel	1.25	0.0672	Seeberger Sandstein	16400	2.05	5100	874	64.0
Xia and Ahrens (2001) shot 108	4.5 (US)	Aluminum	2.8	0.2483	San Marcos gabbro	n.d.	n.d.	1019	129	16.1
Xia and Ahrens (2001) shot 109	4 (US)	Aluminum	2.8	0.2483	San Marcos gabbro	n.d.	n.d.	926	106	14.3
Xia and Ahrens (2001) shot 110	3.5 (US)	Aluminum	2.8	0.2483	San Marcos gabbro	n.d.	n.d.	758	71	12.5
Ai and Ahrens (2004a)	7 (US)	Lead	2.8	1.0429	San Marcos granite	16200	2.66	1200	751	25.0
Polanskey and Ahrens (1990) shot 840901	2 (V)	Aluminum	1.59	0.0443	San Marcos gabbro	11878	2.9	6490	933	12.6
Polanskey and Ahrens (1990) shot 840902	4 (V)	Fe	1.59	0.1292	San Marcos gabbro	11878	2.9	4600	1367	25.2
Polanskey and Ahrens (1990) shot 840904	4.5 (V)	Fe	1.59	0.1297	San Marcos gabbro	11878	2.9	5440	1919	28.3
Polanskey and Ahrens (1990) shot 840905	3.2 (V)	Fe	1.59	0.1297	San Marcos gabbro	11878	2.9	4600	1372	20.1
Polanskey and Ahrens (1990) shot 840906	3.5 (V)	Fe	1.59	0.1297	San Marcos gabbro	11878	2.9	4760	1469	22.0
Polanskey and Ahrens (1990) shot 840907	1.5 (V)	Basalt	2.38	0.1557	San Marcos gabbro	11878	2.9	2260	398	6.3
Polanskey and Ahrens (1990) shot 840909	5 (V)	Steel	3.18	1.0571	San Marcos gabbro	11878	2.9	1690	1510	15.7
Meteor Crater (Ackermann et al. 1975; Roddy et al. 1975)	~80000 (G)	Iron meteorite	~15000-50000	~150 x E + 9	Sandstone, Limestone	n.d.	n.d.	15000	1.9 x E + 16	26.7

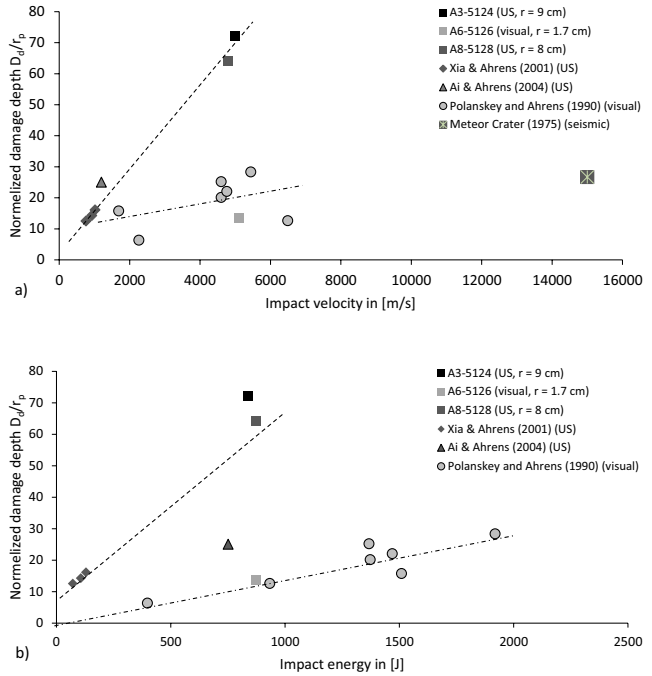

Fig. 8. Plot of the normalized damage depth (D_d/r_p) against the impact velocity (a) and the impact energy (b). Results of 14 different experiments of four research projects are shown together with data from a seismic survey of Meteor Crater (with data of Ackermann et al. 1975) in Fig. 8a. Similar experiments show similar results. For all experiments the damage depth was calculated with US measurement techniques except for Polanskey and Ahrens and for MEMIN target A6-5126 (Buhl et al. 2013) where damage was assessed visually in cross-sections, and for Meteor Crater, where seismic refraction techniques were used. The dashed lines show the increase in the damage of US-based results and the dotted-dashed lines the damage based on visual results.

Crater the crater diameter/damage depth is 1.48. For the MEMIN crater, the crater diameter/damage depth is 0.75–0.81 (crater diameter: 6–6.5 cm, damage depth: 8 cm). With an assumed transient crater diameter of 3.2 cm (Dufresne et al. 2013) crater diameter/damage depth is 0.4. The difference in damage depth relative to the crater diameter may be caused by a potentially higher cratering efficiency in gravity-dominated targets than in strength-dominated targets, or by limitations in the seismic refraction technique that underestimate the damage depth.

Pilkington and Grieve (1992) give a decrease of up to 25% in *p*-wave velocities for the Brent impact crater, Ontario (crystalline target), although this decrease is attributed to the allochthonous breccias lens and not to fractured target rock below the crater. For fractured sedimentary target rocks below the breccias lens at Meteor Crater, a range of decreased velocities from 95 down to 50% was measured (Ackermann et al. 1975). For the US tomography measurements a decrease of 18% (MEMIN A3-5124) and a decrease of 25% (MEMIN A8-5128) are calculated.

Modal Analysis

The modal analysis does not locally resolve the damage zone of an impacted target. Nonetheless it provides an estimation of the damage intensity relative to other damaged and the undamaged targets. The calculated values for the elastic moduli of undamaged Seeberger Sandstein (E_{long} = 14.5 GPa and E_{flex} = 15.3 GPa) agree with the measured value (E = 14.8 GPa; Kenkmann et al. 2011). Both results, calculated with modal analysis and measurements of Kenkmann et al. (2011), are valid for dry sandstone targets. The presented results reflect the elastic parameters of the entire target block and are thus a mixture of undamaged regions and the localized deformation around the impact crater (Figs. 6 and 7). The damage parameter was calculated with Equation 5 and uses the measured frequencies instead of the velocities of all three modes before and after the impact (Table 1). The damage parameter is smaller than the one calculated with the reduction of *p*-wave velocities. The reduction of the frequencies after the impact is much higher for the flexural mode than for the longitudinal and torsional mode. This characteristic is caused by the fact that the flexural mode has two important nodal points, one at 25% and one at 75% of the target's length. The points of maximal oscillation for the first flexural vibration mode are at 0%, 50%, and 100% of the target's length (Figs. 6c and 6d). At around 50%, at the midpoint of the impact crater, the dampening of the vibration is significantly increased. The other vibrational modes (E_{long} and G_{tors}) are not affected this strongly by this behavior. Local information for the elastic modulus needs other nondestructive measuring methods like a calculation with the results of US tomography of compressional (*p*-) and transversal (*s*-) wave velocities.

It should be noted that the decrease in the elastic modulus, calculated with the frequency of the flexural mode, is the same as the decrease in the *p*-wave velocity, i.e., 18%. This result is due to the connection between the wave velocities inside a material and its elastic moduli. Each value can be calculated using one of the other values.

CONCLUSION

On the laboratory scale, NDT methods are well suited to characterize a target before and after an impact cratering experiment. They give information about the extent of damage, fractures, cracks, or other inhomogeneities. The characterization before the impact

allows constraining the damage generated by the impact. In the present article the results of two impact craters are shown.

The major conclusions are:

1. The US tomography revealed a damage zone recognizable as a roughly hemispherical low-velocity zone of the measured *p*-wave velocities (Fig. 3). This zone is much deeper than that one derived by visual evaluations. The US tomography method applied here is capable of detecting fractures that were neither visible in micro-computer tomography measurements, nor in scanning electron microscope analyses performed by Buhl et al. (2013).
2. Micro-computer tomography gives a good overview of large cracks underneath the crater surface of the experimentally impacted target sandstone block (Fig. 5). Fractures were recognized as either spall fractures or "concentric fractures," following the terminology of Polanskey and Ahrens (1990). This is in good agreement with observations of subsurface deformation reported in other MEMIN experiments (Buhl et al. 2013).
3. The target's elastic properties decrease in impacted target. The modal analysis gives only an average for the whole target, and does not locate the damage zone (Figs. 6 and 7). Local variations within the target block cannot be measured with the modal analysis.

For future experiments, a full through-transmission measurement of the whole target before and after the impact experiment is planned allowing better calculation of the damage parameter for individual grid points. For more information a 3-D tomography is needed, but this method requires a much more elaborate set-up, a longer time to complete measurements, and is much more complex in the evaluation of measurements.

A deep understanding of how the acoustic signals translate into a quantitative description of the fracture zone in terms of extent, fracture size, and type of fracture (tensile or shear) is part of ongoing work.

Acknowledgments—The MEMIN research unit FOR 887 and project GR 1664/6-1 are funded by the German Research Foundation DFG. We appreciate the cooperation of the EMI and the assistance of the EMI technicians for the impact experiments. The Bundeswehr Research Institute for Materials, Fuels and Lubricants (WIWeB), especially H. Dinnebier, are gratefully acknowledged for their support with computer tomography measurements. M. Dura, F. Deitert, B. Portner, and F. Reidl are thanked for their help with performing over 20000 handheld single measurements. Special thanks also to J. Morgan, J. Plado, and A. Deutsch for their helpful remarks and assistance.

Editorial Handling—Dr. Alexander Deutsch

REFERENCES

Ackermann H. D., Godson R. H., and Watkins J. S. 1975. A seismic refraction technique used for subsurface investigation at Meteor Crater, Arizona. *Journal of Geophysical Research* 80:765–775.

Ahrens T. J. and Rubin A. M. 1993. Impact-induced tensional failure in rock. *Journal of Geophysical Research* 98:1185–1203.

Ai H. 2006. Shock-induced damage in rocks: Application to impact cratering. Ph.D. thesis, California Institute of Technology, Pasadena, California, USA. 159 p.

Ai H. and Ahrens T. J. 2004a. An experimental tomography study of impact-induced damage beneath craters (abstract #1979). 35th Lunar and Planetary Science Conference. CD-ROM.

Ai H. and Ahrens T. J. 2004b. Dynamic tensile strength of terrestrial rocks and application to impact cratering. *Meteoritics & Planetary Science* 39:233–246.

Ai H. and Ahrens T. J. 2005. Shock-induced damage beneath normal and oblique impact craters (abstract #1243). 36th Lunar and Planetary Science Conference. CD-ROM.

Birch F. 1960. The velocity of compressional waves in rocks to 10 kilobars. *Journal of Geophysical Research* 65:1083–1102.

Buhl E., Poelchau M. H., Dresen G., and Kenkmann T. 2013. Deformation of dry and wet sandstone targets during hyper-velocity impact experiments, as revealed from MEMIN program. *Meteoritics & Planetary Science* 48, doi: 10.1111/j.1945-5100.2012.01431.x.

Donofrio R. R. 1997. Survey of hydrocarbon-producing impact structures in North America: Exploration results to date and potential for discovery in Precambrian basement rock. *Oklahoma Geological Survey Circular* 100:17–29.

Dufresne A., Poelchau M. H., Kenkmann T., Deutsch A., Hoerth T., Schäfer F., and Thoma K. 2013. Crater morphology in sandstone targets: The MEMIN impact parameter study. *Meteoritics & Planetary Science* 48, doi: 10.1111/maps.12024.

Ebert M., Hecht L., Deutsch A., and Kenkmann T. 2013. Chemical modification of projectile residues and target material in a MEMIN cratering experiment. *Meteoritics & Planetary Science* 48, doi: 10.1111/j.1945-5100.2012.1429.x.

Güldemeister N., Durr N., Wünnemann K., and Hiermaier S. 2013. Propagation of impact-induced shock waves in porous sandstone using mesoscale modeling. *Meteoritics & Planetary Science* 48, doi: 10.1111/j.1945-5100.2012.01430.x.

Hoerth T., Schäfer F., Thoma K., Kenkmann T., Poelchau M. H., Lexow B., and Deutsch A. 2013. Hypervelocity impacts on dry and wet sandstone: Observations of ejecta dynamics and crater growth. *Meteoritics & Planetary Science* 48, doi: 10.1111/maps.12044.

Jones R. and Fącąoaru I. 1984. Recommendations for the use of resonant-frequency method in testing concrete specimens. *Materials and Structures* 2:83–86.

Kenkmann T., Wünnemann K., Deutsch A., Poelchau M. H., Schäfer F., and Thoma K. 2011. Impact cratering in sandstone: The MEMIN pilot study on the effect of pore water. *Meteoritics & Planetary Science* 46:890–902.

Kenkmann T., Trullenque G., Deutsch A., Hecht L., Ebert M., Salge T., Schäfer F., and Thoma K. 2013. Deformation and melting of steel projectiles in hypervelocity cratering experiments. *Meteoritics & Planetary Science* 48, doi: 10.1111/maps.12018.

Michael G. 2001. X-ray computed tomography. *Physics Education* 36:442–451.

O'Connell R. and Budiansky B. 1974. Seismic velocities in dry and saturated cracked solids. *Journal of Geophysical Research* 79:5412–5426.

Ohtsu M. 2011. Damage evaluating in freezing and thawing test of concrete by elastic-wave methods. *Material and Structures* 44:1725–1734.

Pesonen L. J. 1996. The impact cratering record of Fennoscandia. *Earth, Moon, and Planets* 72:377–393.

Pilkington M. and Grieve R. A. F. 1992. The geophysical signature of terrestrial impact craters. *Reviews of Geophysics* 30:161–181.

Poelchau M. H., Kenkmann T., Thoma K., Hoerth T., Dufresne A., and Schäfer F. 2013. The MEMIN research unit: Scaling impact cratering experiments in porous sandstones. *Meteoritics & Planetary Science* 48, doi: 10.1111/maps.12016.

Polanskey C. A. and Ahrens T. J. 1990. Impact spallation experiments: Fracture patterns and spall velocities. *Icarus* 87:140–155.

Roddy D. J., Boyce J. M., Colton G. W., and Dial A. L., Jr. 1975. Meteor Crater, Arizona, rim drilling with thickness, structural uplift, diameter, depth, volume, and mass-balance calculations Proceedings, 6th Lunar Science Conference. pp. 2621–2644.

Sommer F., Reiser F., Dufresne A., Poelchau M. H., Hoerth T., Deutsch A., Kenkmann T., and Thoma K. 2013. Ejection behavior characteristics of experimental impacts into dry and wet sandstone: Results from the MEMIN research unit. *Meteoritics & Planetary Science* 48, doi: 10.1111/maps.12017.

Weiler B. and Grosse C. 1995. Elastic constants—Their dynamic measurement and calculation. *Otto-Graf-Journal* 6:116–131.

Xia K. and Ahrens T. J. 2001. Impact induced damage beneath craters. *Geophysical Research Letters* 28:3525–3527.